Check for updates

Fingering Instability During Mixing-Driven Precipitation Flow

Negar Shahsavar[1] · Xiaojing Fu[2] · Benzhong Zhao[1]

Abstract

In this study, we experimentally investigate fluid–fluid displacement in a Hele–Shaw cell where the two fluids react, upon mixing, to form solid precipitates. Under the conditions of our experiments, we observe that precipitation reaction along the moving fluid–fluid interface generates solids in the form of mineral particle suspensions. We find that both electrostatic and hydrodynamic forces control the extent of particle–particle agglomeration during the suspension flow. Such particle suspension decreases the overall mobility of the multiphase mixture, thus altering the overall displacement. Although the injected fluids are viscously stable, the precipitation band that forms between the fluids becomes unstable to form finger-like flow channels compartmentalized by solid-deposited walls and clusters. We show that the emergence, growth and decay of the fingering pattern are strongly influenced by the injection rate and the initial fluid chemical concentrations. In addition, we show that precipitation-induced fingering has a strong feedback on fluid–fluid mixing and the subsequent precipitation rate. Lastly, we find that, counter to intuition, a higher injection rate results in a larger amount of precipitates that are securely deposited in the Hele–Shaw cell.

Keywords Mineral precipitation · Pattern formation · Particle-laden flow

1 Introduction

Reactive flows in porous media that results in precipitation of solids are ubiquitous in a wide range of applications. For example, in physiology, precipitation process leads to kidney stone formation (Walton et al. 1967). In industrial settings, precipitation leads to fouling of porous membrane during water treatment (Matty and Tomson 1988), modification of concrete strength (Zhang et al. 2014), and salinization of agricultural soil (Nachshon et al. 2011a, b; Schoups et al. 2005). In environmental settings, precipitation occurs during infiltration of acid mine drainage into groundwater aquifers (Park et al.

✉ Benzhong Zhao
    robinzhao@mcmaster.ca

1   Department of Civil Engineering, McMaster University, Hamilton, ON L8S 4L8, Canada

2   Department of Mechanical and Civil Engineering, California Institute of Technology, Pasadena, CA 91125, USA

2021) and remediation of groundwater contaminated by dense nonaqueous phase liquids (DNAPLs) via in situ chemical oxidation (Wang et al. 2022).

More recently, the study of mineral precipitation in porous media has received increased attention in the context of geological carbon storage (Jiang and Tsuji 2014; Sigfusson et al. 2015; Matter et al. 2016; Snaebjornsdottir et al. 2017). To this end, many studies have shown that mineralization and precipitation of salts in porous media can decrease the effective permeability and porosity of the rock formation, leading to a significant increase in the pressure drop and a decrease in injectivity and storage capacity (Singurindy and Berkowitz 2023; Peysson et al. 2014; Andre et al. 2014; Ott et al. 2015; Miri and Hellevang 2016). Laboratory studies focusing on microscopic changes of the porous media have elucidated the complexity of the precipitation patterns (Maghraby et al. 2011; Mohamed et al. 2011; Sankur et al. 1986; Krevor et al. 2016; Pentland et al. 2011; Krause et al. 2011) due to the highly nonlinear coupling between advection, diffusion, reaction, and the intrinsic heterogeneity of the pore geometry and mineralogy.

Studying reactive flows in quasi-2D geometry such as a Hele–Shaw cell allows one to directly visualize the coupled flow and reaction process in a relatively simple flow configuration (Haudin et al. 2014; Barge et al. 2015; Cartwright et al. 2002). Using a Hele–Shaw cell setup, it has been shown that varying the reactants, concentrations and injection rates leads to a fascinating array of diverse precipitation patterns that include fingers, spirals, and filaments to name a few (Haudin et al. 2014; Schuszter et al. 2016; Ziemecka et al. 2020). Furthermore, there is a strong feedback from reaction onto the flow, because precipitation often alters the local fluid viscosity and/or the effective permeability of the Hele–Shaw cell (Haudin and De Wit 2015; Sin et al. 2019). By decreasing the local mobility at the interface, the displacement would not be stable, and a hydrodynamic instability arises at the interface (Nagatsu et al. 2014). However, the physical mechanisms behind the coupling between reaction and hydrodynamics, as well as the onset and growth of precipitation-driven fingering remain less well-understood.

Here, we study the displacement of aqueous solutions of calcium chloride by sodium carbonate in a Hele–Shaw cell where the two fluids react, upon mixing, to form calcium carbonate precipitates. We examine the case of equal reactant concentrations in detail via high-resolution imaging, which reveals a variety of precipitation patterns at different injection rates and reactant concentrations. We find that reaction along the moving fluid–fluid interface forms a precipitation band in the form of particle suspensions, whose width and particle concentration are controlled by the injection rate. This injection rate dependent behavior arises due to particle–particle agglomeration in the precipitation band, which occurs when the hydrodynamic force overcomes the electrostatic forces (Perez et al. 2020). Therefore, higher injection rates generate larger particles and lower suspension mobility, resulting in miscible viscous fingering at the precipitation band (Feng et al. 2016). We analyze the emergence, growth and decay of the fingering pattern under different injection rates and initial fluid chemical concentrations. We demonstrate that the temporal growth of precipitation amount is diffusive with time in the *absence* of fingering, but is linear with time in the *presence* of fingering, as explained by recirculatory flow inside the fingertip and supported by simple scaling arguments. Furthermore, we show that the precipitates uniformly deposit onto the top and bottom surfaces of the Hele–Shaw cell as a thin particle layer at low injection rate, but they form large particle islands at high injection rates. Finally, we observe erosion of the deposited particles due to hydrodynamic stresses after sustained injection.

2 Experimental Setup

We study experimentally the reactive flow dynamics of calcium carbonate ($CaCO_3$) precipitation in a Hele–Shaw flow cell, which consists of two glass discs of radius $R_o = 5$ cm separated by a constant gap of thickness $b = 100$ μm (Fig. 1).

The total pore volume of the flow cell is $PV = 0.81$ mL. To perform an experiment, we first fully saturate the cell with an aqueous solution of calcium chloride ($CaCl_2$) (MilliporeSigma). The cell is fully submerged in a reservoir of the same $CaCl_2$ solution. We then inject an aqueous solution of sodium carbonate (Na_2CO_3) (MilliporeSigma) at a constant rate Q using a syringe pump (PHD 4000, Harvard Apparatus), forcing radially outward displacement of $CaCl_2$. We keep the molar concentrations of $CaCl_2$ and Na_2CO_3 solutions equal to c_0 in each experiment, but vary them between different experiments. Mixing between the invading $Na_2CO_{3(aq)}$ and the defending $CaCl_{2(aq)}$ triggers $CaCO_3$ precipitation by the reaction $Na_2CO_{3(aq)} + CaCl_{2(aq)} \rightarrow CaCO_{3(s)}$.

The experiments take place in a dark box, where the only light source is an LED light panel (BK3223, Knema LLC) that uniformly illuminates the flow cell from below. We image the experiment via a 16-bit scientific camera (Orca Flash 4.0, Hamamatsu) mounted directly above the center of the flow cell. The scientific camera has a complementary metal-oxide-semiconductor (CMOS) sensor with 2048×2048 pixels, which yields a spatial resolution of 60 μm per pixel. Precipitation of $CaCO_3$ scatters the incoming light and reduces locally the amount of light reaching the camera. Therefore, the local light intensity indicates the concentration of $CaCO_3$ precipitates semi-quantitatively. We normalize the raw images obtained from the camera using

$$I_{norm} = \frac{1 - I/I_{ref}}{1 - i_{sat}}, \tag{1}$$

where I, I_{ref}, and I_{norm} are matrices of the raw image, the reference image (i.e., image captured before Na_2CO_3 injection), and the normalized image, respectively. i_{sat} is the pixel intensity of regions fully saturated with $CaCO_3$ precipitates. The normalized image therefore illustrates the spatial distribution of precipitate saturation, where pixel intensity $I_{norm} = 0$ indicates regions with no precipitates and $I_{norm} = 1$ indicates regions where the entire gap of the flow cell is saturated with precipitates (Fig. 2).
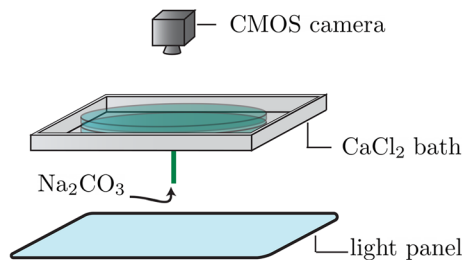
Fig. 1 We study the dynamics of calcium carbonate precipitation in a radial Hele–Shaw cell made of two transparent glass disks separated by $b = 100$ μm-thick shims. The Hele–Shaw cell is initially saturated with calcium chloride and placed in a bath of the same fluid to avoid capillary edge effects. We inject sodium carbonate into the center of the Hele–Shaw cell at a constant rate Q to drive the precipitation of calcium carbonate. We image the experiment from above with a CMOS camera, which captures the change in light intensity due to precipitation

Fig. 2 Precipitation patterns for different injection rates (left to right: $Q = 0.1, 1, 5$ mL/min) and initial concentrations of the reactants (bottom to top: $c_0 = 0.5, 0.75, 1$ mol/L). These patterns correspond to when the precipitation front has reached $\approx 80\%$ of the cell radius. The colormap indicates gap-averaged concentration of precipitates semi-quantitatively
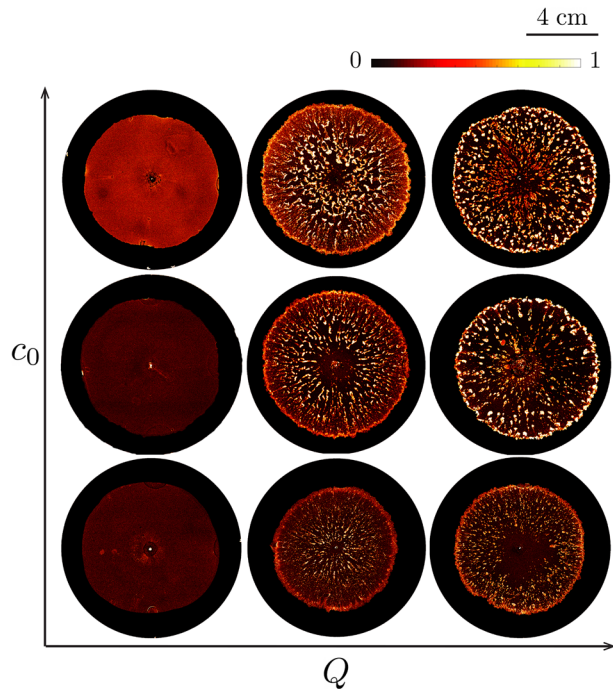
We study the impact of reactant concentration ($c_0 = 0.5$, 0.75, and 1 mol/L) and injection rate ($Q = 0.1$, 1, and 5 mL/min) on the precipitation pattern of $CaCO_3$. The tendency of our system to form $CaCO_3$ precipitation in the absence of flow can be characterized by the saturation index SI $= \log_{10}(IAP/K_{sp})$, where IAP is the ion activity product of the reactant mixture, and $K_{sp} = C^0_{Ca^{2+}} C^0_{CO_3^{2-}}$ is the solubility product of $CaCO_3$, and $C^0_{Ca^{2+}} = C^0_{CO_3^{2-}} = c_0$ are the initial concentration of reactants (Staples and Nuttall 1977; Robinson and Macaskill 1979; Schuszter et al. 2016). The saturation indices in our experiments are much greater than zero (SI $= 7.88, 8.23$, and 8.84), which indicates supersaturation conditions favorable for $CaCO_3$ precipitation (Schuszter et al. 2016; Sand et al. 2016).

3 Results and Discussion

3.1 Experimental Phase Diagram

We present an experimental phase diagram of the final precipitation patterns obtained under different injection rates Q and initial reactant concentrations c_0 (Fig. 2). The colormap of the phase diagram indicates the concentration of the precipitates across the gap of the flow cell inferred from imaging. Intuitively, one would expect the amount of precipitation to increase with increasing c_0. This is indeed the case across all Q. Interestingly, for a given c_0, increasing Q dramatically alters the size, distribution, and gap-averaged concentration of the precipitates. At low Q, we observe the formation of precipitates much smaller than the size of a

single pixel, which are then uniformly deposited over the flow cell. At higher Q, however, we observe the formation of much larger precipitate aggregates, deposited in the flow cell as discrete clusters along the radially outward direction.

In all experiments, $CaCO_3$ precipitation initiates along the $CaCl_2(aq)$–$Na_2CO_3(aq)$ interface, which forms a radial band of precipitation particle suspension (Fig. 3a).
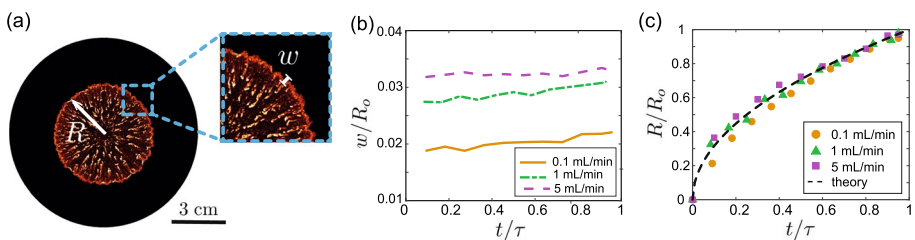
3.2 Precipitation Band Accretion

Precipitation of $CaCO_3$ particles occurs as soon as Na_2CO_3 enters the $CaCl_2$-saturated flow cell. The radial flow profile and accumulation of the particles combine to form a radial precipitation band that moves with the injection velocity for all Q, such that its radius $R(t) = \sqrt{Qt/\pi b}$ (Fig. 3c). Additionally, the width of the precipitation band w remains relatively constant in time, though it does increase with increasing Q (Fig. 3b).

The precipitation band accretion takes full shape at ~ 1 cm away from the injection port. Even at this early stage, the gap-averaged concentration of precipitates is visibly greater at higher Q, as indicated by the image intensity of the precipitation band (Fig. 4a). The high saturation indices of our experiments indicate instantaneous reaction between the reactants, such that $CaCO_3$ precipitation is mixing limited (Haudin and De Wit 2015; De Simoni et al. 2007; Valocchi et al. 2019). We hypothesize that the greater precipitation at higher Q is due to flow detachment and vortex formation at the entrance of the Hele–Shaw cell (Lee and Kang 2020; Stergiou et al. 2022), which enhances mixing and generates more precipitation.

At high Q, in addition to the higher precipitate concentration, we also observe the formation of larger particle aggregates, which act to destabilize the precipitation band (Fig. 5b, c). Here, we hypothesize that larger precipitates clusters are born out of shear-induced aggregation of smaller precipitated particles (Perez et al. 2020). In the absence of flow, the dispersion and agglomeration of particles in confined spaces are controlled by Derjaguin–Landau–Verwey–Overbeek (DLVO) force F_{DLVO}, which consists of electric double-layer repulsion force F_{EDL} (positive) and van der Waals attraction force F_{vdW} (Derjaguin and Landau 1993) (negative). The F_{vdW} between two colloidal particles is given by:

$$F_{vdW} = \frac{-Ar_p}{12d^2}, \tag{2}$$

Fig. 3 **a** We characterize the radial precipitation band by its radius R and width w. **b** Dimensionless band width as a function of dimensionless time for $c_0 = 1$ mol/L experiments at different Q, where $\tau = PV/Q$ is defined as the amount of time it takes to inject 1 pore volume of the invading fluid. **c** The evolution of the dimensionless band position as a function of dimensionless time for $c_0 = 1$ mol/L experiments at different Q. The dashed line indicates the fluid–fluid interface position described by $R/R_o = \sqrt{t/\tau}$
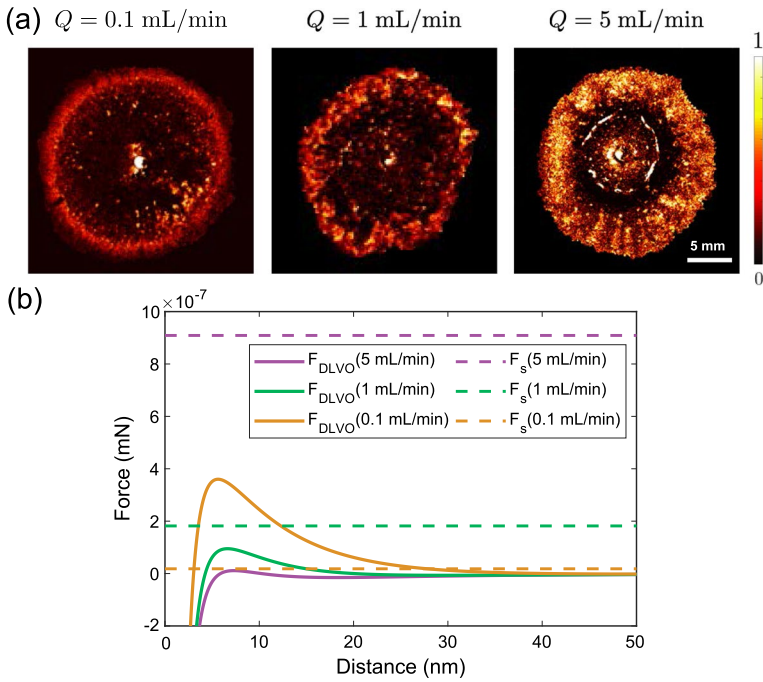
Fig. 4 **a** Precipitation band morphology and intensity 1 cm away from the injection port at different injection rates. The concentrations of CaCl$_2$ and Na$_2$CO$_3$ solutions equal to $c_0 = 0.75$ mol/L. **b** The DLVO force between two CaCO$_3$ particles (solid lines) and the hydrodynamic force (dashed lines) at 1 cm away from the injection point at different injection rates. The hydrodynamic force corresponding to $Q = 0.1$ mL/min is insufficient to overcome the DLVO force

where A is the Hamaker constant, r$_p$ is the radius of particles, and d is the distance between the particle–particle pair (Israelachvili 2011). We use $A = 1.44 \times 10^{-22}$ J, which corresponds to the Hamaker constant value for two CaCO$_3$ particles in water as predicted by the full Lifshitz theory (Bergstrom 1997; Dziadkowiec et al. 2018). We use r$_p$ = 7.7 μm, which corresponds to the experimentally determined initial CaCO$_3$ particle size in a solution with SI = 10 and in near quiescent conditions (Tzachristas et al. 2020).

We calculate the electric double-layer repulsion force F$_{EDL}$ using the Poisson–Boltzmann equation (Israelachvili 2011; Diao and Espinosa-Marzal 2016)

$$\mathrm{F_{EDL}} = 2\pi r_p \epsilon \epsilon_0 \kappa \frac{\psi_c^2 \exp\left(-\kappa d\right) + 2 \exp\left(-2\kappa d\right)((2p_c - 1)\psi_c^2)}{1 - (2p_c - 1)^2 \exp(-2\kappa d)}, \qquad (3)$$

where ψ_c is the CaCO$_3$ surface potential, p_c is the regulation parameter, κ is the inverse Debye length, ϵ is the dielectric constant of the water, and ϵ_0 is the dielectric permittivity of vacuum. The ψ_c, p_c, and κ are sensitive to the ionic composition of the solution (Israelachvili 2011; Diao and Espinosa-Marzal 2016). Therefore, calculation of F$_{EDL}$ requires knowledge of the concentration of the ionic species at the precipitation band. The precipitation band separates regions of high Na$_2$CO$_3$ concentration and low CaCl$_2$ concentration from regions of high CaCl$_2$ concentration and low Na$_2$CO$_3$ concentration. At the precipitation band, Na$_2$CO$_3$ and CaCl$_2$ come into contact through diffusion and form CaCO$_3$ precipitates. Since the precipitation band moves with the injection velocity at all Q, we can solve a

simple set of reaction-diffusion equations to find the evolution of the concentration profiles of Ca^{2+} and CO_3^{2-} ions in the frame comoving with the precipitation band (GaüLlfi and RaüLcz 1988; Paster et al. 2013)

$$\frac{\partial C_{CO_3{}^{2-}}}{\partial t} = D_m \nabla^2 C_{CO_3{}^{2-}} - K C_{CO_3{}^{2-}} C_{Ca^{2+}}, \tag{4}$$

$$\frac{\partial C_{Ca^{2+}}}{\partial t} = D_m \nabla^2 C_{Ca^{2+}} - K C_{Ca^{2+}} C_{CO_3{}^{2-}}, \tag{5}$$

where $D_m = 10^{-9}$ m^2/s is the molecular diffusion coefficient (Yuan-Hui and Gregory 1974) and $K = 10^{3.42}$ m^3/mol $\cdot$ s is the reaction rate constant (Ubbink 2013; Leaist and Noulty 1985; Morse and Mackenzie 1990; Stumm and Morgan 2012). C_α denotes the concentration (in mol/m^3) of ion α. We find that Ca^{2+} and CO_3^{2-} concentrations are in the single-digit millimolar range for all c_0 and Q by the time the precipitation band reaches 1 cm away from the injection port. For $c_0 = 0.75$ mol/L, we estimate $\psi_c = -11.6, -8.62, -7.85$ mV, respectively, for the experiments with $Q = 0.1, 1, 5$ mL/min, while $p_c = 0.62$ for all experiments based on colloidal probe atomic force microscopy measurements of Diao and Espinosa-Marzal (2016). The Debye length is calculated by

$$\kappa^{-1} = \left(\frac{\epsilon_0 \epsilon k_B T}{e^2 \left(\sum_i \rho_{\infty_i} z_i^2 \right)} \right)^{\frac{1}{2}}, \tag{6}$$

where ρ_{∞_i}, e, z_i, k_B, and T are the bulk concentration of each ion at the mixing zone, valency of each ion, Boltzmann constant, and absolute temperature. The corresponding Debye length for the experiments with $c_0 = 0.75$ mol/L are calculated to be $\kappa^{-1} = 4.17, 5.42,$ and 7.7 nm for $Q = 0.1, 1, 5$ mL/min, respectively.

For a given particle–particle pair, the magnitude of F_{EDL} and F_{vdW} are functions of the distance between the particles. The repulsive electric double-layer force acts at a longer-range compared to the attractive van der Waals force, such that the repulsive force barrier must be overcome to bring the particles close enough for aggregation to occur (Israelachvili 2011). Figure 4b shows the DLVO forces at different particle separations for the experimental condition of $c_0 = 0.75$ mol/L and different injection rates. We hypothesize that the repulsive DLVO force can be overcome by the hydrodynamic shear force (Perez et al. 2020; Zaccone et al. 2010), which is a function of the shear rate. The maximum hydrodynamic force F_s pushing two particles together is determined by Husband and Adams (1992)

$$F_s = 6.12 \pi \mu r_p^2 G, \tag{7}$$

where μ is the fluid viscosity, $G = 6v/b$ is the maximum shear rate in a Hele–Shaw cell, and $v = Q/(2\pi Rb)$ is the average local velocity. We find that, at 1 cm away from the injection port, F_s is much lower than the maximum F_{DLVO} required for particle agglomeration in the low injection rate ($Q = 0.1$ mL/min) experiment, and the precipitation band consists of diffuse particles (Fig. 4). In contrast, F_s is greater than the maximum F_{DLVO} in both the intermediate and high injection rate ($Q = 1, 5$ mL/min) experiments, leading to the agglomeration of large particles in the precipitation band (Fig. 4).

3.3 Fingering Instability and Pattern Evolution

Even though the invading and defending fluids are viscosity-matched in our experiments, the generation and accumulation of $CaCO_3$ particles at the invading front give rise to particle-induced viscous fingering at the higher injection rates (Fig. 5b, c). Particle-induced viscous fingering has been observed and studied using a Hele–Shaw cell during immiscible displacement where a particle-laden oil is displacing air (Tang et al. 2000; Feng et al. 2016; Kim et al. 2017; Luo et al. 2018), or during miscible displacement where oil is displacing a particle-laden oil suspension (Sin et al. 2019; Luo et al. 2020). The physical mechanism behind this fingering phenomenon is that the particle-laden suspension has a higher effective viscosity than the pure invading fluid (Tang et al. 2000). While the existing body of literature on this phenomenon focuses on displacing a pre-existing particle suspensions, our experiments demonstrate that, even though the initial defending fluid is particle-free, active generation of particles at the displacement front can also act to destabilize the invading process. We observe the same type of "stubby" fingers (Fig. 6b) as in Feng et al. (2016), which is attributed to the inherently stable displacement of the defending $CaCl_2$ by the more viscous precipitation band.

Figure 5 shows the time evolution of the precipitation pattern at different injection rates with the same initial reactant concentration ($c_0 = 0.75$ mol/L). At the low injection rate ($Q = 0.1$ mL/min), the accreted precipitation band has relatively low precipitate
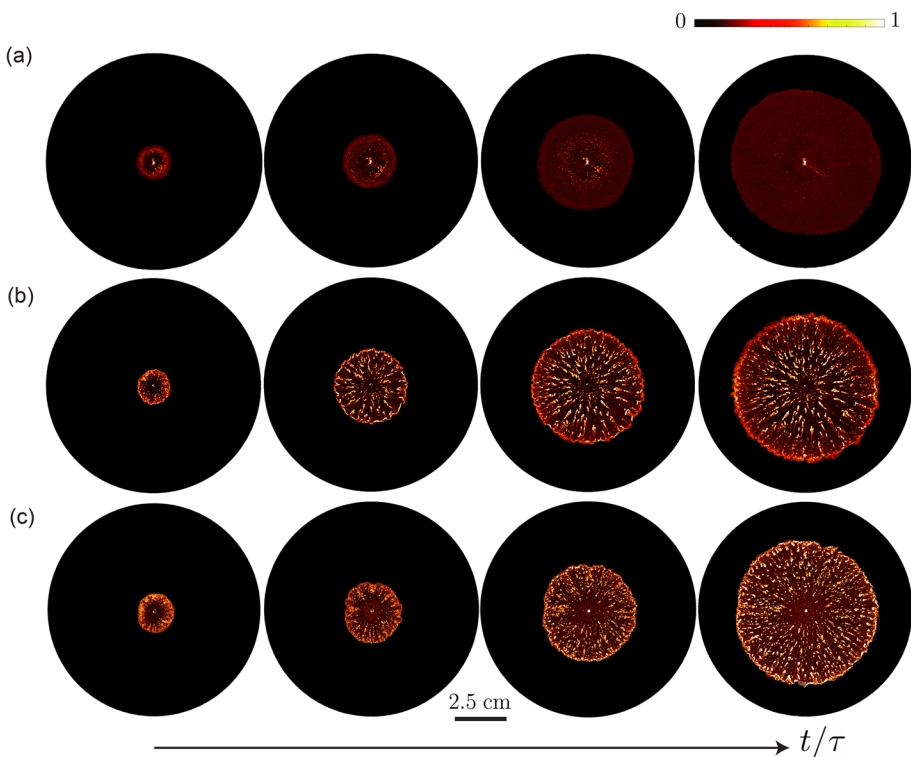
Fig. 5 Evolution of $CaCO_3$ precipitation pattern for different injection rates (top to bottom: $Q = 0.1, 1, 5$ mL/min) at different dimensionless times (left to right: $t/\tau = 0.02, 0.1, 0.25, 0.44$). The concentrations of $CaCl_2$ and Na_2CO_3 solutions equal to $c_0 = 0.75$ mol/L
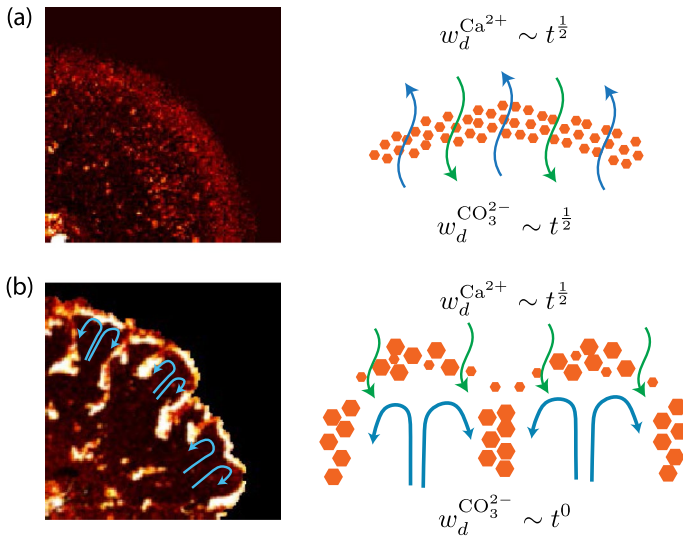
Fig. 6 **a** The depletion zone widths of CO_3^{2-} and Ca^{2+}, defined as the region where the reactant concentrations are significantly smaller than their initial concentration, increase diffusively in time in the absence of fingering. **b** Fingering creates a recirculatory flow that brings fresh Na_2CO_3 solution to the fingertip, such that the concentration of CO_3^{2-} is not depleted and $w_d^{CO_3^{2-}}$ remains constant in time

concentration and small particle size, and fingering is absent throughout the experiment (Fig. 5a). At the high injection rate ($Q = 5$ mL/min), however, the relatively high precipitate concentration and large particle size yield vigorous fingering throughout the experiment (Fig. 5c). At the intermediate injection rate ($Q = 1$ mL/min), fingering is initially evident, but it shuts down as the displacement velocity decreases away from the injection port. This shutdown is accompanied by the apparent decrease in the intensity of the precipitation band (Fig. 5b).

The observed fingering instability also exerts fundamental control over the precipitation rate in our system. We illustrate this effect quantitatively by plotting the evolution of the total normalized intensity $\sum I_{norm}$, which is a measure of the total amount of precipitation in the flow cell. At the low injection rate, the amount of precipitation grows diffusively with time $\sum I_{norm} \sim t^{\frac{1}{2}}$ (Fig. 7a). At the high injection rate, the amount of precipitation grows linearly with time $\sum I_{norm} \sim t$ (Fig. 7c). At the intermediate injection rate, the amount of precipitation grows linearly at early times, but slows down and begins to evolve diffusively after some time, which corresponds to shut down in fingering (Fig. 7b).

We note that similar transition has been observed in radial miscible viscous fingering in the absence of particles (Bischofberger et al. 2014; Chui et al. 2015). Specifically, Chui et al. (2015) found that the length of the mixing zone between the less viscous invading fluid and the more viscous defending fluid grows linearly at early times and diffusively at late times. The physical picture is different in our experiments, however, since the precipitation band remains stable.

We rationalize the observed precipitation trend via simple scaling arguments. Specifically, $CaCO_3$ precipitates form as a result of mixing between Na_2CO_3 and $CaCl_2$ at the precipitation band. The amount of precipitation produced in a unit of time is given by $w\mathcal{R}$, where w is the reaction zone width and $\mathcal{R}$ is the production rate. Gálfi and Rácz (1988)
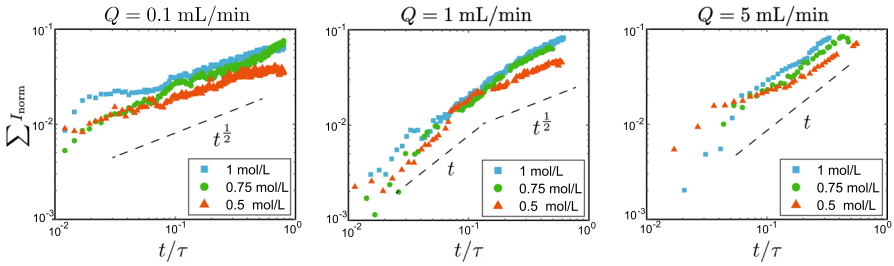
Fig. 7 Evolution of total normalized intensity as a function of dimensionless time for different flow rates. The amount of precipitation grows as $t^{\frac{1}{2}}$ at the low injection rate, but it evolves as t at the high injection rate for all initial concentrations. At the intermediate injection rate, the precipitation growth transitions from t at early times to $t^{\frac{1}{2}}$ at late times, which occurs due to shutdown in miscible viscous fingering

made the scaling assumptions that $w \sim t^{\alpha}$ and $\mathcal{R} \sim t^{-\beta}$. In our system, $w \sim t^0$ since the width of the precipitation band remains constant in time (Fig. 3b). In the frame of reference comoving with the precipitation band, the reactants enter the reaction zone via diffusion, whose fluxes $j_{CO_3^{2-}} \sim j_{Ca^{2+}} \sim c_0/w_d$, where w_d is the width of the depletion zone, defined as the region where the reactant concentrations are significantly smaller than their inital concentration c_0 (GaüLlfi and RaüLcz 1988). It is well-known that the depletion zone width grows diffusively in time (Pillai et al. 1980), such that $j_{CO_3^{2-}} \sim j_{Ca^{2+}} \sim t^{-\frac{1}{2}}$. The average reactant concentration on the reaction front can be estimated as $C_{CO_3^{2-}} \sim w j_{CO_3^{2-}} \sim w t^{-\frac{1}{2}}$ and $C_{Ca^{2+}} \sim w j_{Ca^{2+}} \sim w t^{-\frac{1}{2}}$. Since $CaCO_3$ precipitation is a second order reaction, its production rate can be obtained as $\mathcal{R} \sim t^{-\beta} \sim C_{CO_3^{2-}} C_{Ca^{2+}} \sim w^2 t^{-1} \sim t^{-1}$. In a radial geometry, the perimeter of the precipitation band grows as $\Gamma \sim t^{\frac{1}{2}}$. Finally, the cumulative amount of precipitation is given by

$$M_{CaCO_3}^{low} \approx \int \Gamma w \mathcal{R} dt \sim \int t^{\frac{1}{2}} \cdot t^0 \cdot t^{-1} dt \sim t^{\frac{1}{2}}. \tag{8}$$

This scaling agrees with the measured precipitation evolution in the low injection rate experiments (Fig. 5a).

In the high injection rate experiments, fingering structure incurs recirculation flow within the invading phase (Tan and Homsy 1988; Rocha et al. 2021), which serves to mobilize precipitates away from the fingertip and deposits them along the sides of the finger (Fig. 5b) (Nagatsu et al. 2008). We hypothesize that advection associated with the recirculation flow brings fresh Na_2CO_3 solution to the reaction zone, such that the concentration of carbonate ions near the invading fluid front is not depleted. Therefore, the diffusive flux of carbonate ions $j_{CO_3^{2-}} \sim t^0$. Meanwhile, the depletion zone width of calcium ions in the defending fluid grows diffusively, such that the diffusive flux of calcium ions $j_{Ca^{2+}} \sim t^{-\frac{1}{2}}$. The precipitation rate can be obtained as $\mathcal{R} \sim t^{-\beta} \sim C_{CO_3^{2-}} C_{Ca^{2+}} \sim w^2 t^{-\frac{1}{2}} \sim t^{-\frac{1}{2}}$. Therefore, at high injection rate, the cumulative amount of precipitation is given by

$$M_{CaCO_3}^{high} \approx \int \Gamma w \mathcal{R} dt \sim \int t^{\frac{1}{2}} \cdot t^0 \cdot t^{-\frac{1}{2}} dt \sim t. \tag{9}$$

This scaling agrees with the measured precipitation evolution in the high injection rate experiments (Fig. 5c). The scaling arguments also support the transition from linear to diffusive scaling observed in the intermediate injection rate experiments (Fig. 5b), which occurs when fingering shuts down.

We note that the scaling relations of our experiments differ from that of Gálfi and Rácz (1988), who found $\alpha = \frac{1}{6}$ and $\beta = \frac{2}{3}$ for simple $A + B \rightarrow C$ reactions. In a radial geometry, these exponents predict the cumulative amount of reaction product to scale as $\int \Gamma w \mathcal{R} dt \sim \int t^{\frac{1}{2}} \cdot t^{\frac{1}{6}} \cdot t^{-\frac{2}{3}} dt \sim t$. Brau et al. (2017) demonstrated both experimentally and through theoretical analysis that the scaling exponents of Gálfi and Rácz (1988) still hold for a system subject to passive radial advection. Specifically, Brau et al. (2017) injected an aqueous solution of 0.4 mol/L Na_2CO_3 into an aqueous solution of 0.2 mol/L $CaCl_2$ at a flow rate $Q = 0.1$ mL/min in a radial Hele–Shaw cell with a gap thickness of 500 μm and found $M_{CaCO_3} \sim t$ in the absence of any fingering instability. The key difference of our experiments is the significantly smaller gap thickness of 100 μm, which accentuates the importance of precipitation on reaction and diffusion in the system.

3.4 Precipitation Deposition and Erosion

After the formation of $CaCO_3$ precipitates, some of the particles are advected out of the flow cell, while others deposit inside the cell and alter the porosity and permeability of the flow cell. In the low injection rate experiments, $CaCO_3$ precipitates deposit on the top and bottom surfaces of the flow cell and form a uniform layer due to the electrostatic interactions between the hydrated $CaCO_3$ particles and the glass surface (Durán et al. 1996; Shaik et al. 2021). The $CaCO_3$ layer on the glass surfaces is relatively thin, as evidenced by the low intensity of the precipitation pattern (Fig. 5a). At higher injection rates, larger precipitates form at the fingertip as a result of shear-induced aggregation of smaller particles. Furthermore, the recirculatory flow inside the fingertip brings particles to the sides of the finger. The accumulation of particles at the sides of the finger eventually leads to pinch-off that form discrete islands of trapped particles (Fig. 5b, c). The particle islands are elongated and oriented in the radially outward direction. Therefore, the interplay between hydrodynamics and chemical reaction can significantly alter the porosity and permeability of the flow cell, and it has the capacity to transform an initially homogeneous medium into a heterogeneous one structured with regular preferential pathways.

We investigate the fate of the deposited $CaCO_3$ particles by continuing to inject Na_2CO_3 after the precipitation band reaches the perimeter of the Hele–Shaw cell. At this point, further precipitation ceases since all $CaCl_2$ has been flushed out of the cell. After 3 pore volumes, the difference in the remaining particles are striking—both the amount and size of the precipitates in the high injection rate experiment far exceeds those generated in the lower injection rate experiments (Fig. 8a, b). In addition, we observe erosion of the deposited particles due to hydrodynamic stress exerted by the invading fluid. This is most evident in the high injection rate experiments since the hydrodynamic force increases with the invading fluid velocity and the precipitate particle size squared (Eq. 7). Indeed, we observe significant erosion of the large precipitate islands near the injection port (Fig. 8a right panel).

We plot the evolution of the total normalized intensity $\sum I_{norm}$, and restrict the region of interest (ROI) to $R < 0.8R_o$ to remove noises associated with clamps at the edge of the Hele–Shaw cell. We observe a sharp drop in $\sum I_{norm}$ as the precipitation band leaves the ROI, which is followed by linear decrease in both the high injection rate and intermediate

(a)

(b)

(c)
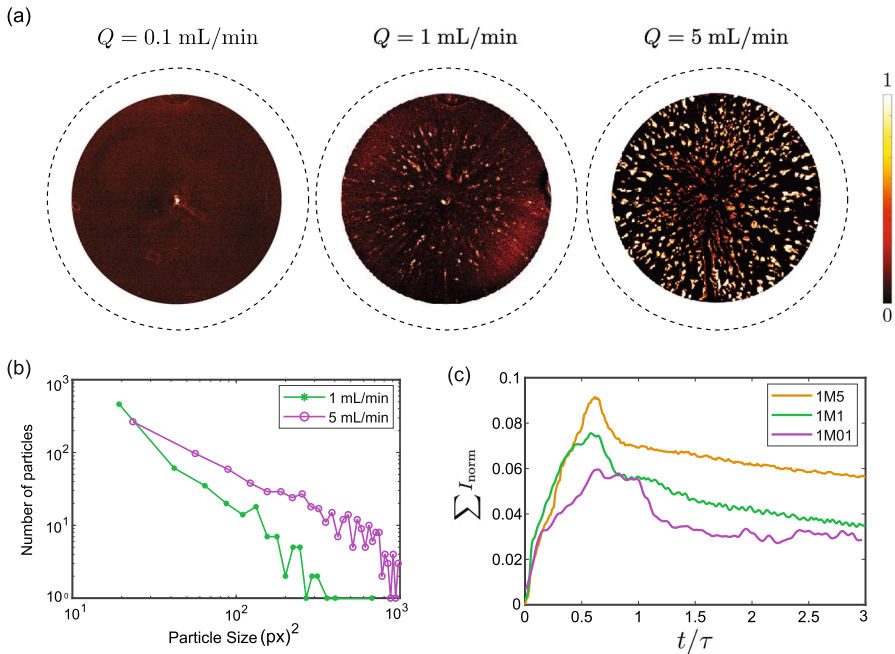
Fig. 8 Long-term behavior of the deposited precipitates after 3 pore volumes of Na_2CO_3 injection. **a** Precipitation deposition pattern. Erosion of the deposited particles due to hydrodynamic stress is evident in the high injection rate experiment near the injection port. **b** Particle size distribution for high and intermediate injection rate experiments. The size of the deposited precipitates in the low injection rate experiments is below the pixel size. **c** Evolution of total normalized intensity as a function of dimensionless time for different injection rates

injection rate experiments (Fig. 8c). The erosion rate in the low injection rate experiment is much gentler, and $\sum I_{norm}$ plateaus after ~ 2 pore volumes.

4 Conclusion

In this study, we experimentally investigate the displacement of $CaCl_2$ by Na_2CO_3 in a Hele–Shaw cell. The reaction between these two fluids, upon mixing, forms a suspension flow consisting of solid $CaCO_3$ precipitates. We vary the injection rates and initial concentrations of the fluids to reveal a variety of precipitation patterns (Fig. 2). We observe that precipitation reaction occurs along the fluid–fluid interface and forms a radial precipitation band that moves with the injection velocity (Fig. 3). The accretion of the precipitation band is strongly influenced by the injection rate—both the amount and size of the particles increase with increasing injection rate (Fig. 4a), which we attribute to enhanced mixing due to cell entrance effect and particle–particle agglomeration due to the interplay between electrostatic and hydrodynamic forces. Specifically, we show that in the cases where the hydrodynamic force overcomes the DLVO force between the particles, it causes them to agglomerate and generates bigger particles (Fig. 4b).

The accumulation of $CaCO_3$ particles at the precipitation band increases the local effective viscosity and consequently leads to particle-induced miscible viscous fingering

instability, even though the two fluids have the same viscosity (Figs. 5, 6). We show that the hydrodynamic instability exerts fundamental control over the total amount of precipitation, which grows as $t^{\frac{1}{2}}$ in the *absence* of fingering, but it evolves as t in the *presence* of fingering (Fig. 7). We attribute this interesting finding to the recirculatory flow inside the finger tip, which constantly brings fresh Na_2CO_3 to the precipitation band (Fig. 6); without the recirculatory flow, the concentrations of both Na_2CO_3 and $CaCl_2$ are depleted diffusively. Our simple scaling arguments agree with the experimental findings. We note that our results differ from the well-established scaling relationship for simple $A + B \rightarrow C$ reactions in radial Hele–Shaw cells, which highlight the important feedback precipitated particles have on reaction and diffusion in the system.

While the precipitation band is advected radially outwards, some of the precipitates deposit inside the cell. At a low injection rate, the deposited particles form a thin layer on the top and bottom surfaces of the flow cell. Interestingly, a higher injection rate leads to a larger amount of precipitates that are securely deposited in the Hele–Shaw cell. This occurs as a result of shear-induced aggregation of smaller particles that accumulate at the sides of the fingers due to recirculatory flow, which eventually pinch off to form discrete precipitate islands that span the entire gap of the flow cell (Fig. 5). Further injection beyond 1 pore volume induces erosion of the deposited particles due to hydrodynamic stress exerted by the invading fluid (Fig. 8). In the context of a natural porous rock, the deposition of thin $CaCO_3$ layer on the surface of solid grains can gradually decrease the pore throat size, while the deposition of larger aggregates of $CaCO_3$ have the potential to completely block the pore space (Perez et al. 2020), significantly decreasing the local permeability and alter the flow paths (Bizmark et al. 2020; Wu et al. 2023). Our results illustrate the complex interplay between mixing, reaction, and hydrodynamic instability in mineral precipitation, which could have important implications in predicting the evolution of permeability and injectivity in CO_2 mineralization projects.

Declarations

Competing interests The authors have no relevant financial or non-financial interests to disclose.

References

Andre, L., Peysson, Y., Azaroual, M.: Well injectivity during CO2 storage operations in deep saline aquifers. Part 2: numerical simulations of drying, salt deposit mechanisms and role of capillary forces, Int. J. Greenh. Gas Control. **22**, 301 (2014)

Barge, L.M., Cardoso, S.S., Cartwright, J.H., Cooper, G.J., Cronin, L., De Wit, A., Doloboff, I.J., Escribano, B., Goldstein, R.E., Haudin, F., et al.: From chemical gardens to chemobrionics. Chem. Rev. **115**, 8652 (2015)

Bergstrom, L.: Hamaker constants of inorganic materials. Adv. Colloid Interface Sci. **70**, 125 (1997)

Bischofberger, I., Ramachandran, R., Nagel, S.R.: Fingering versus stability in the limit of zero interfacial tension. Nat. Commun. **5**, 1 (2014)

Bizmark, N., Schneider, J., Priestley, R.D., Datta, S.S.: Multiscale dynamics of colloidal deposition and erosion in porous media. Sci. Adv. **6**, eabc2530 (2020)

Brau, F., Schuszter, G., De Wit, A.: Flow control of A+ B→C fronts by radial injection. Phys. Rev. Lett. **118**, 134101 (2017)

Cartwright, J.H., García-Ruiz, J.M., Novella, M.L., Otálora, F.: Formation of chemical gardens. J. Colloid Interface Sci. **256**, 351 (2002)

Chui, J.Y., de Anna, P., Juanes, R.: Interface evolution during radial miscible viscous fingering. Phys. Rev. E **92**, 041003 (2015)

De Simoni, M., Sanchez-Vila, X., Carrera, J., Saaltink, M.: A mixing ratios-based formulation for multi-component reactive transport. Water Resour. Res. **43** (2007)

Derjaguin, B.V., Landau, L.D.: Theory of the stability of strongly charged lyophobic sols and of the adhesion of strongly charged particles in solutions of electrolytes. Prog. Surf. Sci. **43**, 30 (1993)

Diao, Y., Espinosa-Marzal, R.M.: Molecular insight into the nanoconfined calcite–solution interface. Proc. Natl. Acad. Sci. USA **113**, 12047 (2016)

Durán, J.D.G., Ontiveros, A., Delgado, A.V., González-Caballero, F., Chibowski, E.: A study on the adhesion of calcium carbonate to glass. Energy balance in the deposition process. J. Adhes. Sci. Technol. **10**, 847 (1996)

Dziadkowiec, J., Javadi, S., Bratvold, J.E., Nilsen, O., Royne, A.: Surface forces apparatus measurements of interactions between rough and reactive calcite surfaces. Langmuir **34**, 7248 (2018)

El-Maghraby, R.M., Pentland, C.H., Blunt, M.J.: Coreflood measurements of CO2 trapping. In: SPE Annual Technical Conference and Exhibition (OnePetro, 2011)

Feng, X., Kim, J., Lee, S.: Particle-induced viscous fingering. J. Nonnewton. Fluid Mech. **238**, 92404 (2016)

Gálfi, L., Rácz, Z.: Properties of the reaction front in an A+ B→C type reaction-diffusion process. Phys. Rev. A **38**, 3151 (1988)

Haudin, F., De Wit, A.: Patterns due to an interplay between viscous and precipitation-driven fingering. Phys. Fluids **27**, 113101 (2015)

Haudin, F., Cartwright, J.H., Brau, F., DeWit, A.: Spiral precipitation patterns in confined chemical gardens. Proc. Natl. Acad. Sci. USA **111**, 17363 (2014)

Husband, J., Adams, J.: Shear-induced aggregation of carboxylated polymer latices. Colloid Polym. Sci. **270**, 1194 (1992)

Israelachvili, J.N.: Intermolecular and Surface Forces (Academic Press, 2011)

Jiang, F., Tsuji, T.: Changes in pore geometry and relative permeability caused by carbonate precipitation in porous media. Phys. Rev. E **90**, 053306 (2014)

Kim, J., Xu, F., Lee, S.: Formation and destabilization of the particle band on the fluid–fluid interface. Phys. Rev. Lett. **118**, 074501 (2017)

Krause, M., Perrin, J.-C., Benson, S.M., et al.: Modeling permeability distributions in a sandstone core for history matching coreflood experiments. SPE J **16**, 768 (2011)

Krevor, S., Reynolds, C., Al-Menhali, A., Niu, B.: The impact of reservoir conditions and rock heterogeneity on CO2-brine multiphase flow in permeable sandstone. Petrophysics **57**, 12 (2016)

Leaist, D.G., Noulty, R.A.: Multicomponent diffusion of aqueous sodium carbonate and aqueous sodium bicarbonate. Can. J. Chem **63**, 2319 (1985)

Lee, S.H., Kang, P.K.: Three-dimensional vortex-induced reaction hot spots at flow intersections. Phys. Rev. Lett. **124**, 144501 (2020)

Luo, R., Chen, Y., Lee, S.: Particle-induced miscible fingering: continuum limit. Phys. Rev. Fluids **5**, 094301 (2020)

Luo, R., Chen, Y., Lee, S.: Particle-induced viscous fingering: review and outlook. Phys. Rev. Fluids **3**, 110502 (2018)

Matter, J.M., Stute, M., SnabjoüNrnsdottir, S.O., Oelkers, E.H., Gislason, S.R., Aradottir, E.S., Sigfusson, B., Gunnarsson, I., Sigurdardottir, H., Gunnlaugsson, E., et al.: Rapid carbon mineralization for permanent disposal of anthropogenic carbon dioxide emissions. Science **352**, 1312 (2016)

Matty, J.M., Tomson, M.B.: Effect of multiple precipitation inhibitors on calcium carbonate nucleation. Appl. Geochem. **3**, 549 (1988)

Miri, R., Hellevang, H.: Salt precipitation during CO2 storage.a review. Int. J. Greenh. Gas Control **51**, 136 (2016)

Mohamed, I.M., He, J., Nasr-El-Din, H.A.: Permeability change during CO2 injection in carbonate rock: a coreflood study. In: SPE Production and Operations Symposium (OnePetro, 2011)

Morse, J.W., Mackenzie, F.T.: Geochemistry of Sedimentary Carbonates (Elsevier, 1990)

Nachshon, U., Shahraeeni, E., Or, D., Dragila, M., Weisbrod, N.: Infrared thermography of evaporative fluxes and dynamics of salt deposition on heterogeneous porous surfaces. Water Resour. Res. **47** (2011)

Nachshon, U., Weisbrod, N., Dragila, M.I., Grader, A.: Combined evaporation and salt precipitation in homogeneous and heterogeneous porous media. Water Resour. Res. **47** (2011)

Nagatsu, Y., Bae, S.-K., Kato, Y., Tada, Y.: Miscible viscous fingering with a chemical reaction involving precipitation. Phys. Rev. Lett. **77**, 067302 (2008)

Nagatsu, Y., Ishii, Y., Tada, Y., De Wit, A.: Hydrodynamic fingering instability induced by a precipitation reaction. Phys. Rev. Lett. **113**, 024502 (2014)

Ott, H., Roels, S., De Kloe, K.: Salt precipitation due to supercritical gas injection: I. capillary driven flow in unimodal sandstone. Int. J. Greenh. Gas Control **43**, 247 (2015)

Park, S., Anggraini, T.M., Chung, J., Kang, P.K., Lee, S.: Microfluidic pore model study of precipitates induced by the pore-scale mixing of an iron sulfate solution with simulated groundwater. Chemosphere **271**, 129857 (2021)

Paster, A., Bolster, D., Benson, D.: Particle tracking and the diffusion-reaction equation. Water Resour. Res. **49**, 1 (2013)

Pentland, C., El-Maghraby, R., Georgiadis, A., Iglauer, S., Blunt, M.: Immiscible displacements and capillary trapping in CO2 storage. Energy Procedia **4**, 4969 (2011)

Perez, A.J., Patino, J.E., Soos, M., Morales, V.L.: Morphology of shear-induced colloidal aggregates in porous media: consequences for transport, deposition, and re-entrainment. Environ. Sci. Technol. **54**, 5813 (2020)

Peysson, Y., Andre, L., Azaroual, M.: Well injectivity during CO2 storage operations in deep saline aquifers. Part 1: experimental investigation of drying effects, salt precipitation and capillary forces. Int. J. Greenh. Gas Control. **22**, 291 (2014)

Pillai, K.M., Vaidyan, V., Ittyachan, M.: On the theory of liesegang phenomena. Colloid Polym. Sci. **258**, 831 (1980)

Robinson, R., Macaskill, J.: Osmotic coefficients of aqueous sodium carbonate solutions at 25 C. J Solut. Chem. **8**, 35 (1979)

Rocha, L.A., Cartwright, J.H., Cardoso, S.S.: Filament dynamics in planar chemical gardens. Phys. Chem. Chem. Phys. **23**, 5222 (2021)

Sand, K., Tobler, D., Dobberschutz, S., Larsen, K., Makovicky, E., Andersson, M., Wolthers, M., Stipp, S.: Calcite growth kinetics: dependence on saturation index, Ca^{2+}: CO_3^{2-} activity ratio, and surface atomic structure. Cryst. Growth Des. **16**, 3602 (2016)

Sankur, V., Creek, J., Dijulio, S., Emanuel, A.: A laboratory study of wilmington tar zone CO2 injection project. SPE Reserv. Eng. **1**, 95 (1986)

Schoups, G., Hopmans, J.W., Young, C.A., Vrugt, J.A., Wallender, W.W., Tanji, K.K., Panday, S.: Sustainability of irrigated agriculture in the San Joaquin Valley, California. Proc. Natl. Acad. Sci. USA **102**, 15352 (2005)

Schuszter, G., Brau, F., De Wit, A.: Calcium carbonate mineralization in a confined geometry. Environ. Sci. Technol. Lett. **3**, 156 (2016)

Schuszter, G., Brau, F., De Wit, A.: Flow-driven control of calcium carbonate precipitation patterns in a confined geometry. Phys. Chem. Chem. Phys. **18**, 25592 (2016)

Shaik, I.K., Zhang, L., Pradhan, S., Kalkan, A.K., Aichele, C.P., Bikkina, P.K.: A parametric study of layer-by-layer deposition of CaCO3 on glass surfaces towards fabricating carbonate reservoirs on microfluidic chips. J. Pet. Sci. Eng. **198**, 108231 (2021)

Sigfusson, B., Gislason, S.R., Matter, J.M., Stute, M., Gunnlaugsson, E., Gunnarsson, I., Aradottir, E.S., Sigurdardottir, H., Mesfin, K., Alfredsson, H.A., et al.: Solving the carbon-dioxide buoyancy challenge: the design and field testing of a dissolved CO2 injection system. Int. J. Greenh. Gas Control. **37**, 213 (2015)

Sin, S., Suekane, T., Nagatsu, Y., Patmonoaji, A.: Three-dimensional visualization of viscous fingering for non-newtonian fluids with chemical reactions that change viscosity. Phys. Rev. Fluids **4**, 054502 (2019)

Singurindy, O., Berkowitz, B.: Evolution of hydraulic conductivity by precipitation and dissolution in carbonate rock. Water Resour. Res. **39** (2003)

Snaebjornsdottir, S.O., Oelkers, E.H., Mesfin, K., Aradottir, E.S., Dideriksen, K., Gunnarsson, I., Gunnlaugsson, E., Matter, J.M., Stute, M., Gislason, S.R.: The chemistry and saturation states of subsurface fluids during the in situ mineralisation of CO2 and H2S at the carbfix site in sw-iceland. Int. J. Greenh. Gas Control. **58**, 87 (2017)

Staples, B.R., Nuttall, R.L.: The activity and osmotic coefficients of aqueous calcium chloride at 298.15 k. J. Phys. Chem. Ref. Data **6**, 385 (1977)

Stergiou, Y., Eckert, K., Schwarzenberger, K.: Entrance effects in a radial Hele–Shaw cell: numerical and experimental study. J. Chem. Eng. **428**, 131146 (2022)

Stumm, W., Morgan, J.J.: Aquatic Chemistry: Chemical Equilibria and Rates in Natural Waters (Wiley, 2012)

Tan, C., Homsy, G.: Simulation of nonlinear viscous fingering in miscible displacement. Phys. Fluids **31**, 1330 (1988)

Tang, H., Grivas, W., Homentcovschi, D., Geer, J., Singler, T.: Stability considerations associated with the meniscoid particle band at advancing interfaces in Hele–Shaw suspension flows. Phys. Rev. Lett. **85**, 2112 (2000)

Tzachristas, A., Malamoudis, R.-I., Kanellopoulou, D.G., Skouras, E., Parthenios, J., Koutsoukos, P.G., Paraskeva, C.A., Sygouni, V.: Mineral scaling in microchips: effect of substrate wettability on $CaCO_3$ precipitation. Ind. Eng. Chem. Res. **59**, 20201 (2020)

Ubbink, B.: Controlled precipitation of calcium carbonate in spatial dimension with multiple calcium chloride and sodium carbonate pulses, Masterüfs thesis, Delft University of Technology (2013)

Valocchi, A.J., Bolster, D., Werth, C.: Mixing-limited reactions in porous media. Transp. Porous. Med. **130**, 157 (2019)

Walton, A.G., Furedi, H., Elving, P.J., Kolthoff, I.M.: The Formation and Properties of Precipitates, Vol. 23 (Interscience Publishers New York, 1967)

Wang, Z., Yang, Z., Fagerlund, F., Zhong, H., Hu, R., Niemi, A., Illangasekare, T., Chen, Y.-F.: Pore343 scale mechanisms of solid phase emergence during DNAPL remediation by chemical oxidation. Environ. Sci. Technol. **56**, 11343 (2022)

Wu, T., Yang, Z., Hu, R., Chen, Y.-F.: Three-dimensional visualization reveals pore-scale mechanisms of colloid transport and retention in two-phase flow. Environ. Sci. Technol. **57**, 1997 (2023)

Yuan-Hui, L., Gregory, S.: Diffusion of ions in sea water and in deep-sea sediments. Geochim. Cosmochim. Acta. **38**, 703 (1974)

Zaccone, A., Gentili, D., Wu, H., Morbidelli, M.: Shear-induced reaction-limited aggregation kinetics of Brownian particles at arbitrary concentrations. Chem. Phys. **132**, 134903 (2010)

Zhang, Y., Guo, H., Cheng, X.: Influences of calcium sources on microbially induced carbonate precipitation in porous media. Mater. Res. Innov. **18**, S2 (2014)

Ziemecka, I., Brau, F., DeWit, A.: Confined direct and reverse chemical gardens: influence of local flow velocity on precipitation patterns. Chaos **30**, 013140 (2020)